Combustion and Flame 205 (2019) 231–240

Contents lists available at ScienceDirect

Combustion and Flame

journal homepage: www.elsevier.com/locate/combustflame

The breakdown of self-similarity in electrified counterflow diffusion flames

Mario Di Renzo[a,b], Giuseppe Pascazio[b], Javier Urzay[a,*]

[a] Center for Turbulence Research, Stanford University, Stanford, CA 94305-3024, United States
[b] Dipartimento di Meccanica, Matematica e Management & Centro di Eccellenza in Meccanica Computazionale, Politecnico di Bari, Bari 70125, Italy

ARTICLE INFO

Article history:
Received 5 October 2018
Revised 27 November 2018
Accepted 2 April 2019

Keywords:
Diffusion flames
Counterflow burners
Electric-fields
Ionic wind

ABSTRACT

This work addresses the question of the validity of self-similar formulations in describing the structures of methane/air laminar counterflow diffusion flames subjected to incident sub-breakdown DC electric fields. The electric field is induced by two flat porous electrodes located on the oxidizer and fuel sides of the burner and arranged parallel to the mixing layer. Both experiments and numerical simulations of this configuration in recent work suggest the presence of a strong coupling effect between the aerothermochemical and electric fields whereby the velocity field is significantly modified by the momentum carried by a bi-directional ionic wind directed axially outwards from the diffusion flame. However, as shown in this study, such strong coupling is incompatible with standard self-similar formulations of the problem. An a-priori analysis of the steady axisymmetric numerical simulations results in Di Renzo et al. (2018) [1], which employ multi-component transport and detailed chemical kinetics, is presented in this study in order to address the suitability of self-similar descriptions in the present configuration. It is shown that, while self-similarity is preserved in unelectrified conditions along radial distances similar to one orifice radius, it breaks down profusely in electrified conditions as the applied voltage increases and nears saturation conditions, where the electric force field becomes two-dimensional and non-conservative in the close vicinity of the burner axis. As a result, for the purposes of self-similarity, increasing electrification counteracts the slenderness of the counterflow burner and decreases its effective aspect ratio. Counterflow burners should therefore be extra slender if preservation of self-similar conditions is sought under incident electric fields.

1. Introduction

Extinction, active control and variation of the lift-off height of a diffusion flame are just few of the possible applications of electric-field effects on combustion [2–5]. In connection with the investigation of fundamental physical mechanisms involved in these phenomena, recent experimental work [6] has shown that a methane/air counterflow diffusion flame subject to a steady voltage difference undergoes non-trivial changes and may become unstable as a result of a strong coupling between the aerothermochemical and electric fields (see Fig. 1 for the burner schematics). Some of these effects involve: (a) a shift of the flame position toward the fuel injector; (b) a variation of the flame curvature with the applied voltage; and (c) the existence of a non-monotonic trend of the electric current density produced by the flame with respect to the applied voltage. These interactions can be explained in terms of imbalances of the electric force exerted on the flow by the positive and negative ions produced in the flame [1,6,7]. In particular, as the applied voltage increases, the numerical simulations in Ref. [1] indicate that a reduction of the local strain rate occurs as a result of a flow-displacement effect imparted by a bi-directional ionic wind directed towards both injectors, which renders a faster chemistry and consequently smaller concentrations of charged species, thereby leading to a decrease in the electric current at intermediate voltages upon electric saturation.

Self-similar descriptions of reacting flows in counterflow burners are the basis of flamelet turbulent combustion models for unelectrified diffusion flames [8–12]. Self-similarity is expressed in a variety of ways in counterflow burners. For instance, at high Reynolds numbers, the flow becomes self-similar in the vicinity of the mixing layer that is formed near the stagnation plane between the two streams and which is much smaller than the separation distance L between the injectors, with the relevant strain rate being the local one at the edges of the mixing layer [13–15].

* Corresponding author.
E-mail addresses: mariodr@stanford.edu (M. Di Renzo), giuseppe.pascazio@poliba.it (G. Pascazio), jurzay@stanford.edu (J. Urzay).

https://doi.org/10.1016/j.combustflame.2019.04.004
0010-2180/

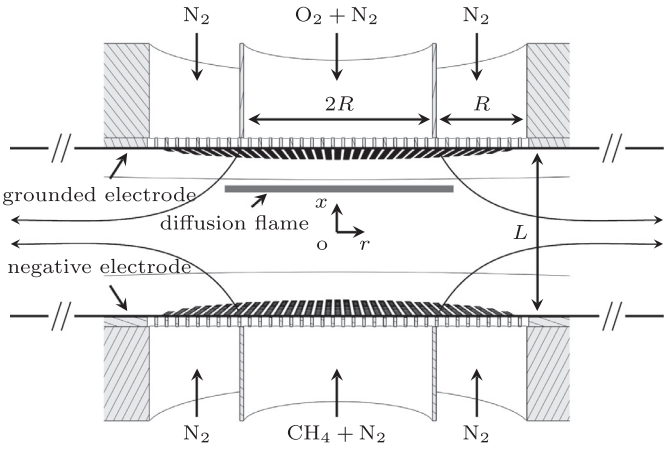

Fig. 1. Sketch of the burner geometry and computational setup (not to scale). The two circular porous electrodes are represented by the horizontal thick solid lines and their radii are equal to $8R$. The aspect ratio of the burner is $2R/L = 1$. Plug-flow boundary conditions are utilized at the injectors. The axisymmetric coordinate system $\{r, x\}$ is placed at mid distance between the two orifice exits (see Refs. [1] and [6] for details).

In porous burners at finite Reynolds numbers, self-similarity is observed in most of the flow field between the injectors and up to radial distances of order $r \sim L$, provided that the burner is geometrically slender, $2R/L \gg 1$, with R being the orifice radius [16]. In all cases, self-similar descriptions are convenient from an operational standpoint, since they involve the integration of ordinary differential equations as opposed to the large computational expenses needed for integrating the full conservation equations in partial differential form [17–20]. However, self-similar formulations have been hardly explored within the context of electrified diffusion flames. In combustion problems involving electric-field effects, the alternative of integrating the full conservation equations is a costly one, since the spatiotemporal resolution requirements are much more stringent because of the large disparities between the scales associated with the bulk neutral gas and those associated with the charged species. Nonetheless, the results presented below suggest that the aforementioned strong aerodynamic coupling observed in Refs. [1] and [6] is incompatible with standard self-similar formulations of counterflow diffusion flames.

Based on these considerations, two fundamental questions arise: (a) to what extent the numerical simulations [1] of the experimental setup utilized in Ref. [6] comply with the necessary constraints for self-similarity of the flow field? (b) is the observed strong aerodynamic coupling a manifestation of the fact that the solution of this problem in this setup necessarily violates self-similarity? Answers to these questions are provided below based on a brief a-priori analysis of the steady axisymmetric numerical simulations described in Ref. [1], which employ multi-component transport and detailed chemical kinetics for methane/air combustion augmented with charged species. The reader is therefore referred to Ref. [1], including its Supplementary Material, for further details on the configuration, conservation equations, chemical kinetics, transport models, numerical methods, and associated boundary conditions.

The analysis in this study is focused on one of the two cases measured in Ref. [6] and simulated in Ref. [1], which employs methane and oxygen streams diluted with nitrogen in such a way that the stoichiometric mixture fraction is $Z_{st} = 0.50$. This case is characterized by a geometrically centered diffusion flame with smaller curvature, and in principle provides the most favorable conditions for self-similarity. Results are also provided in the accompanying Supplementary Material that addresses the additional case $Z_{st} = 0.07$ corresponding to undiluted methane burning in air, as studied in Refs. [1] and [6]. This supplementary case is much less favorable for self-similarity due to the resulting larger values of the flame curvature that necessarily induce radial variations in all variables even close to the burner axis.

The anticipated answers to the two questions outlined above are that the resulting flow is, at most, only locally self-similar at radial distances smaller than the orifice radius in the unelectrified case. However, in electrified cases, where a voltage difference across the electrodes is applied, the region where the flow is locally self-similar rapidly becomes increasingly narrower around the burner axis and vanishes altogether as the voltage increases. Even a self-similar description localized exactly at the burner axis becomes untenable due – among other reasons described below – to significant axial variations of the radial curvature of the pressure profile there. In electrified conditions, the present setup is not particularly amenable to being described by self-similar formulations because of deleterious two-dimensional electrohydrodynamic effects initiated at the edges of the diffusion flame. The results suggest that, in practical applications, counterflow burners chosen for studying electrified diffusion flames should be extra slender if self-similar conditions are to be preserved. These aspects are discussed below.

The remainder of this paper is divided into two sections. A self-similar description of the problem is provided in Section 2 along with an assessment of its validity using an a-priori analysis of the steady axisymmetric numerical simulations of the case $Z_{st} = 0.50$ reported in Ref. [1]. Concluding remarks are given in Section 3. Lastly, a Supplementary Material is appended to this manuscript that contains results of a similar analysis performed for the additional case $Z_{st} = 0.07$.

2. Results

The analysis begins by considering what the formulation of the problem would be in a self-similar description. An assessment of the hypotheses leading to that description is provided thereafter.

2.1. Formulation

Standard assumptions required to derive self-similar descriptions in counterflow combustion problems are: (a) linearly varying radial velocities with the radial coordinate, and as a consequence from continuity, radially independent axial velocities; (b) radially independent distributions of scalars including temperature, density, and mass fractions; and (c) quadratically varying hydrodynamic pressures in the radial direction, with a proportionality constant that is independent of the axial direction [13,17–20]. In the present study, these assumptions have to be necessarily augmented with one that states radial uniformity of the electric potential and charge density.

Following these assumptions, consider the dimensionless velocity components in the axial and radial directions given, respectively, by $\mathcal{U}(\xi) = u_x/U$ and $\mathcal{A}(\xi) = 2u_r/(Ar)$. In the notation, $A = U/L$ is a characteristic strain rate based on the injection velocity U, which is the same for both injectors, and on the gap distance L between the injectors. In addition, the symbol $\xi = x/L$ represents a normalized axial coordinate. Note that an axial similarity coordinate could be defined instead based on a Howarth–Dorodnitsyn type of transformation, and a stream function could be introduced that would make the continuity equation unnecessary, but here $\mathcal{U}$, $\mathcal{A}$ and ξ are employed directly for simplicity.

The velocity components $\mathcal{U}$ and $\mathcal{A}$ are determined by the solution to the transformed conservation equations of mass and radial

momentum, namely

$$\frac{d}{d\xi}(\mathcal{R}\mathcal{U}) + \mathcal{R}\mathcal{A} = 0, \tag{1}$$

$$\mathcal{R}\mathcal{U}\frac{d\mathcal{A}}{d\xi} + \frac{\mathcal{R}\mathcal{A}^2}{2} = J + \frac{1}{Re_L}\frac{d}{d\xi}\left(\hat{\eta}\frac{d\mathcal{A}}{d\xi}\right). \tag{2}$$

These equations need to be integrated simultaneously with

$$\mathcal{R}\mathcal{U}\frac{dY_i}{d\xi} = -\frac{1}{Re_L Pr Le_i}\frac{d}{d\xi}\left(\mathcal{R}\mathcal{V}_{\xi,i}Y_i\right) + Da_i\mathcal{R}\Omega_i \qquad (i = 1, \ldots, N_s), \tag{3}$$

$$c\mathcal{R}\mathcal{U}\frac{d\Theta}{d\xi} = \frac{1}{Re_L Pr}\frac{d}{d\xi}\left(\hat{\lambda}\frac{d\Theta}{d\xi}\right) - \mathcal{R}\sum_{i=1}^{N_s} Da_i\mathcal{H}_i\Omega_i - \frac{\mathcal{R}}{Re_L Pr}\sum_{i=1}^{N_s}\frac{Y_i c_i \mathcal{V}_{\xi,i}}{Le_i}\left(\frac{d\Theta}{d\xi}\right) - \frac{\Xi_E}{Re_L Pr}\sum_{i=1}^{N_s}\frac{\mathcal{R}_{i,q}\mathcal{V}_{\xi,i}}{Le_i}\left(\frac{d\varphi}{d\xi}\right), \tag{4}$$

and

$$\frac{d^2\varphi}{d\xi^2} = -\sum_{i=1}^{N_s}\mathcal{R}_{i,q}, \tag{5}$$

which correspond, respectively, to the transformed conservation equations of species and enthalpy, and the transformed Gauss equation for the electrostatic potential. The above equations are supplemented with the ideal-gas equation of state

$$\mathcal{R}\mathcal{W}\Theta = 1. \tag{6}$$

In this formulation, $\mathcal{R}(\xi) = \rho/\rho_0$, $\mathcal{W}(\xi) = \overline{W}/\overline{W}_0$, $\Theta(\xi) = T/T_0$, $\hat{\eta}(\xi) = \eta/\eta_0$, $\hat{\lambda}(\xi) = \lambda/\lambda_0$, and $c(\xi) = c_p/c_{p0}$ are, respectively, the density, mean molecular weight, temperature, dynamic viscosity, thermal conductivity, and specific heat of the mixture normalized with the corresponding oxidizer-stream value indicated by the subindex $_0$. In addition, among the N_s species in the mixture, variables related to the particular species i are the mass fraction $Y_i(\xi)$ and the normalized values of the specific heat $c_i(\xi) = c_{p,i}/c_{p0}$, the partial specific enthalpy $\mathcal{H}_i(\xi) = h_i/(c_{p0}T_0)$, and the chemical production rate $\Omega_i(\xi) = \dot{w}_i t_{ch,i}$, the latter being nondimensionalized with the inverse of a characteristic chemical time $t_{ch,i}$. Similarly, $\mathcal{V}_{\xi,i} = V_{x,i}L/D_{i0}$ represents a normalized axial diffusion velocity of species i based on the corresponding mass diffusivity at oxidizer-stream conditions D_{i0}, and is given by

$$\mathcal{V}_{\xi,i}(\xi) = -\frac{\hat{D}_i}{X_i}\left(\frac{dX_i}{d\xi}\right) - \Xi_{S,i}\mathcal{S}_i\hat{\mu}_i\frac{d\varphi}{d\xi} + \sum_{j=1}^{N_s} Y_j\alpha_{ji0}\left(\frac{\hat{D}_j}{X_j}\frac{dX_j}{d\xi} + \Xi_{S,j}\mathcal{S}_j\hat{\mu}_j\frac{d\varphi}{d\xi}\right), \tag{7}$$

where $X_i(\xi)$ is the molar fraction, $\hat{D}_i(\xi) = D_i/D_{i0}$ and $\hat{\mu}_i(\xi) = \mu_i/\mu_{i0}$ are the normalized mass diffusivity and mobility, respectively, and $\alpha_{ji0} = D_{j0}/D_{i0}$ are ratios of mass diffusivities at oxidizer-stream conditions. Additionally, $\mathcal{S}_i$ is the number of elementary charges expressed as a multiple of the absolute value of the electron charge e. In the present configuration, and under the chemical-kinetic modeling assumptions utilized in Ref. [1], $\mathcal{S}_i = +1$ for the ions H_3O^+ and CHO^+, and $\mathcal{S}_i = -1$ for the electrons e^- and for the anions O_2^-, O^-, and OH^-.

The classic aerothermochemical coupling in the above equations is quantified by the non-dimensional parameters $Pr = \nu_0/D_{T0}$, $Le_i = D_{T0}/D_{i0}$, $Da_i = (At_{ch,i})^{-1}$, and $Re_L = UL/\nu_0$, which represent, respectively, the Prandtl, Lewis, Damköhler, and Reynolds number. In the notation, ν_0 and D_{T0} correspond, respectively, to the kinematic viscosity and thermal diffusivity of the oxidizer stream. In this configuration, the Reynolds number Re_L is moderately large, $Re_L = 126$, in such a way that the flow remains laminar [6] (note there is a factor of 2 discrepancy with respect to the Re_L value quoted in Ref. [1] due to a redefinition of the characteristic strain rate A made here for convenience of the notation as one half of that defined previously there). Correspondingly, heat conduction, mass transport, and viscous stresses are important within the mixing layer that is formed near the stagnation plane. In non-reacting conditions, the thickness of the mixing layer is smaller than L by a factor of order $Re_L^{-1/2} \ll 1$. It should however be noted that the temperature increase resulting from the exothermic chemical reactions involves an increase in the local kinematic viscosity near the stagnation plane, which, in practice, leads to an increase in the thickness of the mixing layer to amounts of order $L/2$ no longer small compared with L (i.e., see Figs. 5 and 6 in Ref. [1]).

In writing Eq. (2), the hydrodynamic pressure has been assumed to have the customary functional form [13,17–20]

$$\frac{p}{\rho_0 U^2} = \pi(\xi) - \frac{J}{4}\left(\frac{r}{L}\right)^2. \tag{8}$$

As described below, the function $\pi(\xi)$ enters passively in the axial momentum equation and does not play any role in the determination of the velocity field. In contrast, $J = -(\rho_0 A^2 r/2)^{-1}(\partial p/\partial r)$ is a positive constant independent of the spatial coordinates that is proportional to the radial curvature of the pressure profile and is required for the computation of the velocity components, as in Eq. (2). For instance, in a symmetric constant-density potential flow, $J = 1/2$ as demanded by Eq. (2) since $\mathcal{A} = 1$ everywhere. In the present configuration, plug-flow boundary conditions for the velocity are employed, which are motivated by the use of contoured nozzles and interposed perforated-plate electrodes in the experiments, and by the absence of quantitative experimental characterizations of the velocity field near the nozzles in this burner [1,6,7]. As a result, J becomes an eigenvalue of the problem to be determined as part of the solution of the third-order system of equations (1) and (2) while imposing the four inflow-velocity boundary conditions (i.e., $\mathcal{U} = -1$ at $\xi = +1/2$, $\mathcal{U} = 1$ at $\xi = -1/2$, and $\mathcal{A} = 0$ at $\xi = \pm 1/2$). At sufficiently high Reynolds numbers $Re_L \gg 1$, the resulting eigenvalue is

$$J = 2\left(1 + \sqrt{\rho_F/\rho_0}\right)^2, \tag{9}$$

with ρ_F being the density of the fuel stream. This expression can be analytically derived by integrating Eqs. (1) and (2) in the two inviscid regions formed by the impinging jets away from the mixing layer, which, in the limit $Re_L \gg 1$, becomes a tangential discontinuity located at the stagnation plane. This procedure yields piecewise velocity profiles on the oxidizer and fuel sides of the stagnation plane with six constants of integration. These constants, along with J, can be determined using the four aforementioned kinematic boundary conditions, the mechanical-equilibrium condition that the radial pressure gradient is equal on both sides of the stagnation plane, along with two non-penetration conditions at the stagnation plane for the two piecewise distributions of the axial velocity [18].

An important role in the above equations, which sets them apart from those typically used in unelectrified counterflow diffusion flames [13,18,21], is played by the dimensionless electrostatic potential $\varphi(\xi) = \Phi/|\Delta\Phi_0|$ and by the dimensionless version of the electric charge density $\rho_{q,i} = \rho N_A e \mathcal{S}_i Y_i/W_i$, denoted as $\mathcal{R}_{i,q}(\xi) = \rho_{q,i}L^2/(\epsilon_0\Delta\Phi_0)$. In these expressions, $\Delta\Phi_0$ is the voltage difference imposed across the electrodes, N_A is the Avogadro

number, W_i is the molecular weight of species i, and ϵ_0 is the vacuum permittivity.

According to the formulation above, the coupling between the electric and aerothermochemical fields occurs through the last term on the right-hand side of the enthalpy equation (4), which corresponds to an Ohmic dissipation, and through the second and last components of the diffusion velocity (7), which represent electrodiffusion mechanisms of charged species. The latter participate in the mass diffusion of species in Eq. (3), as well as in the heat transfer by species interdiffusion represented by the second term on the right-hand side of Eq. (4). These couplings for energy and species transport are quantified, respectively, by the two dimensionless parameters

$$\Xi_E = \frac{(\Delta\Phi_0)^2\epsilon_0}{\rho_0 c_{p0} T_0 L^2} \quad \text{and} \quad \Xi_{S,i} = \frac{\mu_{i0}|\Delta\Phi_0|}{D_{i0}}. \tag{10}$$

In the simulations performed in Ref. [1], $\Xi_E \sim 10^{-8} - 10^{-7} \ll 1$ is a very small parameter, thereby indicating that the effect of the Ohmic dissipation on the temperature field is negligible.

In contrast, $\Xi_{S,i} \sim 10^3 - 10^4 \gg 1$ is a large parameter for all tested voltages. Based on the Einstein relation employed in Eq. (S1.18) in Ref. [1] for the direct proportionality between binary mobilities and binary mass diffusivities, and on the relations in Eqs. (S1.14) and (S1.19) in Ref. [1] between binary and individual values of the mobilities and mass diffusivities, the parameter $\Xi_{S,i}$ can be rewritten as

$$\Xi_{S,i} = \Xi_S = \frac{|\Delta\Phi_0|}{\kappa_B T_0/e}, \tag{11}$$

which is independent of the species index i. The large value of $\Xi_{S,i}$ therefore indicates that the applied voltages $|\Delta\Phi_0| = O(1\text{ kV})$ are much larger than the characteristic thermal voltage $\kappa_B T_0/e \sim 25$ mV, with κ_B being the Boltzmann constant. As a result, the charged species are highly susceptible to diffusion by electromigration, as described by the second and fourth terms that comprise the diffusion velocity (7). Note that the largeness of $\Xi_{S,i}$ in (7) is compensated by the smallness of Re_L^{-1} in Eq. (3), thereby suggesting that electromigration is dominant within the mixing layer, where the charged species are generated, and where convection balances ordinary molecular diffusion. However, electromigration is not necessarily confined to the mixing layer, as shown in the charged species distributions in Fig. 7 of Ref. [1], where long tails in the concentration of H_3O^+ and O_2^- are observed, respectively, on the fuel and oxidizer sides of the stagnation plane in the inviscid region in the form of a bi-directional ionic wind. This can be understood in terms of dimensionless parameters by noticing that, upon combining Eqs. (3) and (7), the prefactor $\Xi_{S,i}/(Re_L Pr Le_i) \sim 10$–$100$ multiplying the electromigration flux is generally much larger than unity, thereby enabling the motion of charges by electromigration across scales of order L with corresponding velocities larger than U. Note that, whereas the Lewis numbers of the heavy ions are not too different from unity (i.e., $Le_{CHO^+} = 1.65$, $Le_{H_3O^+} = 1.12$, $Le_{O_2^-} = 1.24$, $Le_{OH^-} = 0.80$, and $Le_{O^-} = 0.79$), the Lewis number of the electrons $Le_{e^-} = 0.002$ is small because of their high mobility, or equivalently, their large diffusivity. Correspondingly, the dimensionless group $\Xi_{S,e^-}/(Re_L Pr Le_{e^-})$ is particularly large for electrons. Nonetheless, electrons are rapidly consumed in electron-attachment chemical reactions that involve conversion of O_2, OH, and O into their ionized counterparts, and therefore the electrons rarely survive away from the mixing layer.

Regarding their effects on the velocity components, it is however important to note that the couplings quantified by the dimensionless parameters Ξ_E and $\Xi_{S,i}$ lead, at most, to weak modifications of the density, temperature, and composition fields of major species [1]. The rather mild character of this coupling rests upon the following facts: (a) the gas is very weakly ionized under the incident sub-breakdown electric fields utilized here, with electron number densities being of order 10^{11} cm^{-3}; and (b) no electric coupling terms appear explicitly in the mass and radial momentum equations (1) and (2). In particular, no radial electric force is involved in the momentum balance (2), since the electric potential φ must necessarily be assumed to be a sole function of the axial coordinate ξ as a result of the radial uniformity of the mass fractions Y_i of charged species in the self-similar formulation.

In contrast, the electric force, which is dimensionally defined as $\mathbf{f_{el}} = -\sum_{i=1}^{N_s} \rho_{q,i} \nabla\Phi$, is axially directed as prescribed by its proportionality to the gradient of the potential and only participates passively in the conservation equation of axial momentum, namely

$$\mathcal{R}\mathcal{U}\frac{d\mathcal{U}}{d\xi} = -\frac{d\pi}{d\xi} + \frac{1}{Re_L}\left\{\hat{\eta}\frac{d\mathcal{A}}{d\xi} + \frac{4}{3}\frac{d}{d\xi}\left[\hat{\eta}\left(\frac{d\mathcal{U}}{d\xi} - \frac{\mathcal{A}}{2}\right)\right]\right\} + \mathcal{F}_{\mathrm{el},\xi}, \tag{12}$$

where

$$\mathcal{F}_{\mathrm{el},\xi}(\xi) = \frac{\mathrm{f}_{\mathrm{el},x}}{\rho_0 UA} = -\Xi_M \sum_{i=1}^{N_s} \mathcal{R}_{q,i}\frac{d\varphi}{d\xi} \tag{13}$$

is the dimensionless axial component of the electric force, and

$$\Xi_M = \frac{(\Delta\Phi_0)^2\epsilon_0}{\rho_0 U^2 L^2}, \tag{14}$$

is a dimensionless momentum-coupling parameter that measures the ratio of the characteristic convective acceleration to the electric force per unit volume.

According to Eq. (12), the uniform and purely axial electric force (13) can be absorbed – without any dynamical consequences whatsoever – into the gradient of a modified hydrodynamic pressure $p^\star/(\rho_0 U^2) = \pi^\star(\xi) + (J/4)(r/L)^2$, where $\pi^\star(\xi)$ is given by

$$\pi^\star(\xi) = \pi(\xi) - \int_0^\xi \mathcal{F}_{\mathrm{el},\xi}(\xi)\,d\xi. \tag{15}$$

Note that $\pi(\xi)$ or $\pi^\star(\xi)$ are both inconsequential for the solution of the velocity field and can be directly computed by integrating Eq. (12) supplemented with the known distributions $\mathcal{U}(\xi)$, $\mathcal{A}(\xi)$, $\Theta(\xi)$, $\varphi(\xi)$, and $Y_i(\xi)$ obtained by solving Eqs. (1)–(5). Such effortless absorption of the electric force into the hydrodynamic pressure gradient is a manifestation of the principle of extended Galilean invariance, and can only be made possible if the electric force is conservative, as is necessarily the case for the uniform and purely axial electric force (13) encompassed by the self-similar formulation outlined above. As a result, according to Eqs. (1)–(13), the bi-directional ionic wind of H_3O^+ and O_2^- resulting from electromigration fluxes directed away from the mixing layer should be powerless in exerting any influence on the velocity field. Remarkably, this should occur regardless of the value of the dimensionless coupling parameter Ξ_M that is defined in (14) and premultiplies the electric force (13), insofar as Ξ_M remains much smaller than the square of the inverse of the Mach number

$$Ma = \frac{U}{\sqrt{(\gamma_0 - 1)c_{p0}T_0}} = O(10^{-3}) \ll 1 \tag{16}$$

in order to preserve the uniformity of the thermodynamic pressure in the present low-Mach approximation, where γ_0 is the adiabatic coefficient in the oxidizer stream.

In contrast, the numerical results presented in Figs. 8 and 9 in Ref. [1], obtained by integrating the full conservation equations, suggest the following: (a) the axial electric force (13) is comparable or larger than the characteristic convective force $\rho_0 UA$; and (b) the associated momentum exchanged by the bi-directional ionic wind and the bulk neutral gas causes significant modifications of

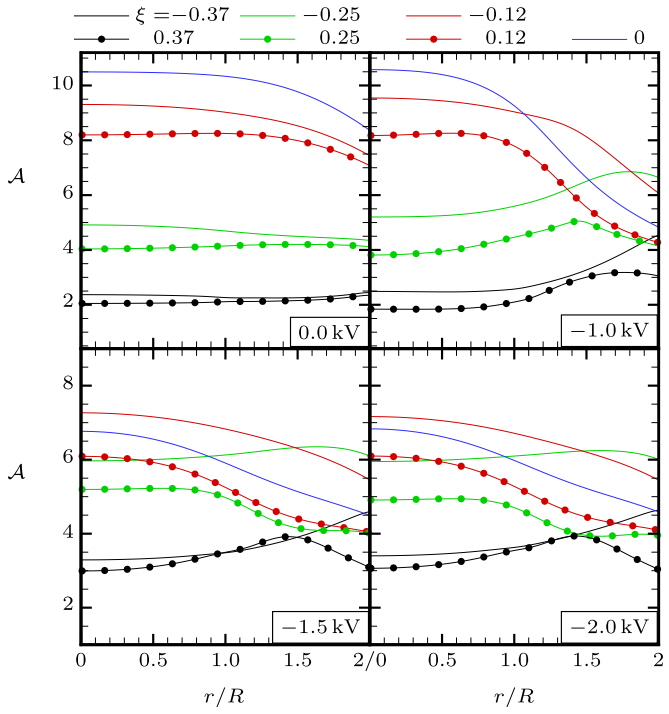

Fig. 2. Radial profiles of the transformed radial velocity for the case $Z_{st} = 0.50$.

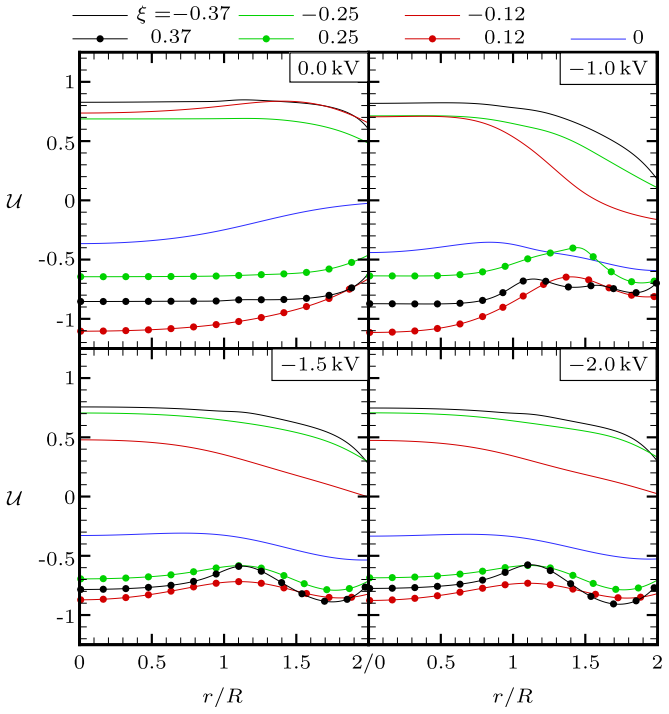

Fig. 3. Radial profiles of the transformed axial velocity for the case $Z_{st} = 0.50$.

the axial velocity field across the burner by momentum transfer. Similar flow modifications were observed in the experiments reported in Ref. [6], although there the strength of the interaction appears to be superior to that obtained from the numerical simulations because of possible reasons discussed in Ref. [1]. In both experiments and simulations, the dimensionless coupling parameter Ξ_M in Eq. (14) is of order unity. However, as mentioned above, this strong momentum coupling is incompatible with the self-similar description (1)–(13), where the electric force is just passively absorbed into the hydrodynamic pressure gradient.

Based on the above considerations, there must exist noticeable discrepancies between the simulation results presented in Ref. [1] and the hypotheses that lead to Eqs. (1)–(13). These are investigated in what follows.

2.2. A-priori analysis of numerical simulations

The analysis of the simulation results in Ref. [1], where the full (untransformed) conservation equations are integrated in steady axisymmetric form, indicates that the radial extent of the region where self-similarity holds becomes increasingly narrower as the voltage increases. This is illustrated in Figs. 2–5, which show, respectively, the profiles of $\mathcal{A}$, $\mathcal{U}$, J, and Θ as a function of the radial coordinate normalized with the injector orifice radius R at different axial positions ξ. In interpreting these results, it is convenient to notice that the diffusion flame is approximately located within the interval $-0.1 \lesssim \xi \lesssim 0.05$ in all cases.

Necessary requirements for Eqs. (1)–(12) to hold are therefore that $\mathcal{A}$, $\mathcal{U}$, and Θ should be independent of r for every ξ, and that J should be independent of both r and ξ. In equivalent form, u_x and T should be one-dimensional fields that only depend on x, and u_r and $\partial p/\partial r$ should scale linearly with r, with the multiplicative factor of the latter being independent of x. These requirements are noticeably satisfied for $r/R \lesssim 1$ and all ξ in the unelectrified case with $Z_{st} = 0.50$, and they are violated in the same case radially away from the burner axis where $r/R \gtrsim 1$.

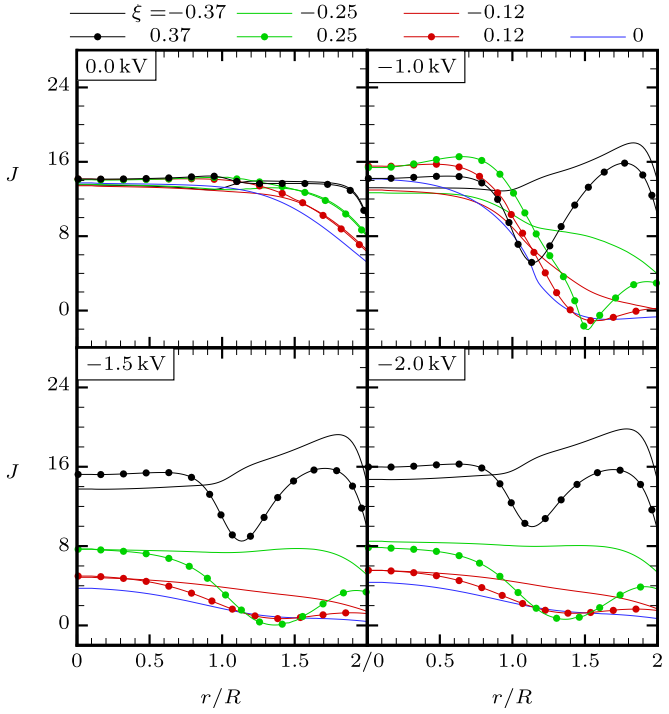

Fig. 4. Radial profiles of the transformed radial pressure gradient for the case $Z_{st} = 0.50$.

In unelectrified conditions, the transformed radial pressure gradient J near the axis is approximately uniform, but, as illustrated in Fig. 6, its value is nonetheless nearly twice that predicted by Eq. (9) (i.e., $J \approx 7.35$, since $\rho_F = 0.84\rho_0$ in these simulations). The cause of this discrepancy lies in the insufficiently high value of the Reynolds number used in this configuration, which renders a relatively thick mixing layer in reacting conditions due to the local increase of the kinematic viscosity in the vicinity of the

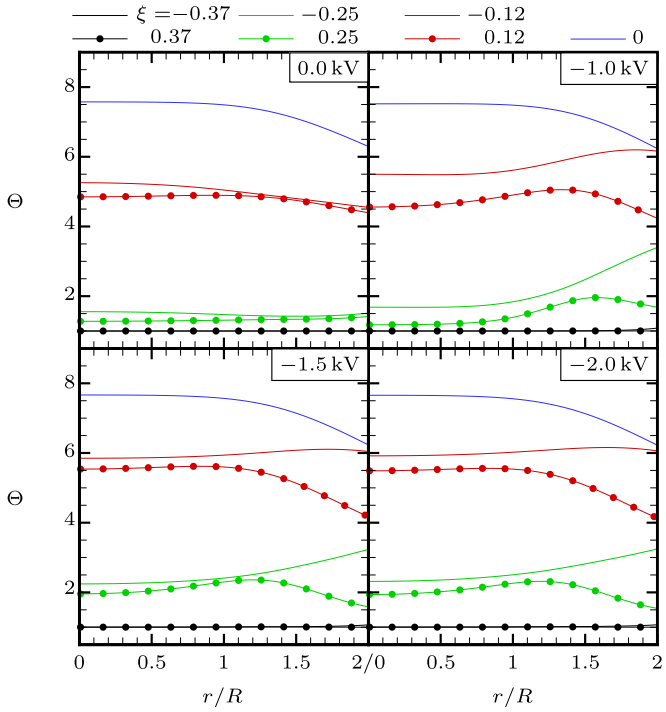

Fig. 5. Radial profiles of the normalized temperature for the case $Z_{st} = 0.50$.

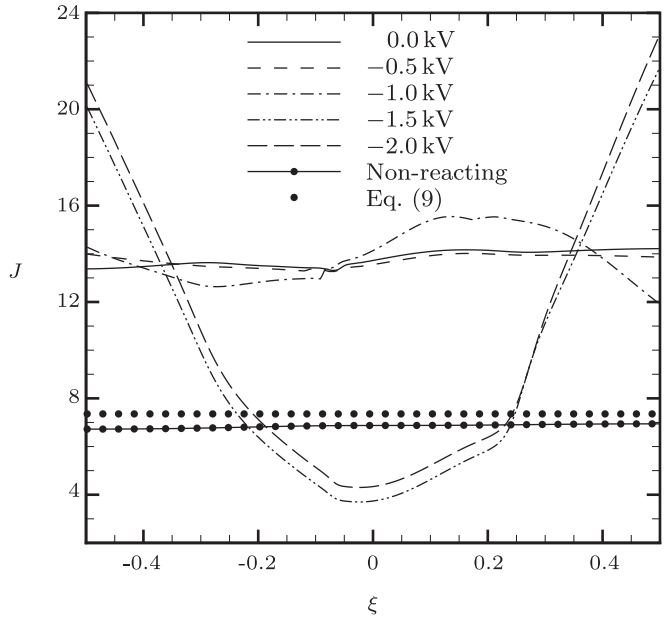

Fig. 6. Axial distribution of the transformed radial pressure gradient J along the axis $r = 0$ for the case $Z_{st} = 0.50$.

diffusion flame (e.g., see axial temperature profiles in Fig. 5 in Ref. [1]). Instead, as shown in Fig. 6, the theoretical value of J given by Eq. (9) is best reproduced in non-reacting conditions.

In the case under investigation, the diffusion flame, which remains notably flat, has a diameter of approximately $4R$ (i.e, see Fig. 10(b) in Ref. [1]) and therefore penetrates in the range of radial distances where the iso-velocity nitrogen curtain is injected. This range corresponds to $1 \leq r/R \leq 2$. As a result, the formulation (1)–(13) is generally not applicable for $r/R = O(1)$ even in the unelectrified case, particularly near the injectors, where the density $\mathcal{R}$ and mass fractions Y_i necessarily become a function of the radial coordinate.

Most importantly, however, is that the constancy of u_x and T with r, along with the linear scalings of u_r and $\partial p/\partial r$ with r, which are observed in the unelectrified case in the region $r/R \lesssim 1$ for all ξ, are all rapidly degraded and increasingly more confined to the vicinity of the axis as the voltage increases. For instance, no clear self-similar region can be discerned in Figs. 2–5 in the cases −1.5 and −2.0 kV.

As the voltage increases, an evident mismatch of the hydrodynamic pressure occurs with respect to the form assumed in Eq. (8), as illustrated in Figs. 4 and 6. In particular, as the voltage increases, the transformed radial pressure gradient J near the axis ceases to have an approximately uniform value and becomes an increasingly more pronounced function of both ξ and r. Specifically, as shown in Fig. 6, a strong parabolic dependence of J on ξ in electrified conditions is observed along the burner axis $r = 0$, where self-similar descriptions often find the most and only suitable region to be deployed.

The undesirable presence of an axially varying curvature of the radial pressure profile in this problem is reminiscent of a similar phenomenon found in Refs. [22] and [23] on unelectrified combustion problems in counterflow burners with the same aspect ratio $2R/L = 1$ than the present one. In those, the breakdown of self-similarity is typically attributed to the flow two-dimensionality induced by the lack of geometrical slenderness of the burner [24]. In contrast, in the present configuration, the unelectrified solution complies well with the self-similar description for $r/R \lesssim 1$ because of the particular chemical composition of the injectants that favors a nearly flat diffusion flame placed near the geometrical center of the burner. However, a clear breakdown of self-similarity occurs as the voltage increases which is caused by two-dimensional flow effects initiated by the electric field at the edges of the diffusion flame, as described below.

2.2.1. Low voltages

At low voltages below saturation $|\Delta\Phi_0| \lesssim 1.0$ kV, the radial profiles of the electric potential have two well-differentiated plateaus for every ξ away from the electrodes, as shown in Fig. 7. On one hand, the outer plateau corresponds to the axially linear distribution of electric potential $\varphi = \xi - 1/2$ resulting from applying the voltage difference across the electrodes while sandwiching the non-ionized gas found radially far away from the diffusion flame. On the other hand, the inner plateau constitutes a large disturbance of the outer linear distribution of electric potential and is introduced by the shielding action of the charged species, and more particularly, H_3O^+ and O_2^-. These, in sub-saturated conditions, are produced at an abundant rate in comparison with the rate at which they are removed outwardly from the diffusion flame by the electromigration flux. As a result, the distribution of the normalized total electric-charge density $\mathcal{R}_q = \sum_{i=1}^{N_s} \mathcal{R}_{q,i}$ has sharp horizontal ridges above and below the diffusion flame where charges accumulate axially in a shield-like manner, as shown in the two upper left contour maps in Fig. 8 (see also the axial profiles of charge density in Fig. 3 in Ref. [1]).

Each of the two plateaus in the electric potential leads to corresponding regions of approximate uniformity in the axial electric force, as shown in Fig. 9. In the outer plateau, $\mathcal{F}_{\mathrm{el},\xi}$ is small due to the absence of charges. In the inner plateau, and away from the mixing layer, $\mathcal{F}_{\mathrm{el},\xi}$ attains dimensional values comparable or larger than the characteristic convective force $\rho_0 UA$. In the self-similar description (1)–(13), however, these large values of $\mathcal{F}_{\mathrm{el},\xi}$ are inconsequential for the velocity distribution and do not lead to any aerodynamic coupling, since the effect of $\mathcal{F}_{\mathrm{el},\xi}$ is passively absorbed into the hydrodynamic pressure gradient without any dynamical consequences, as stressed above.

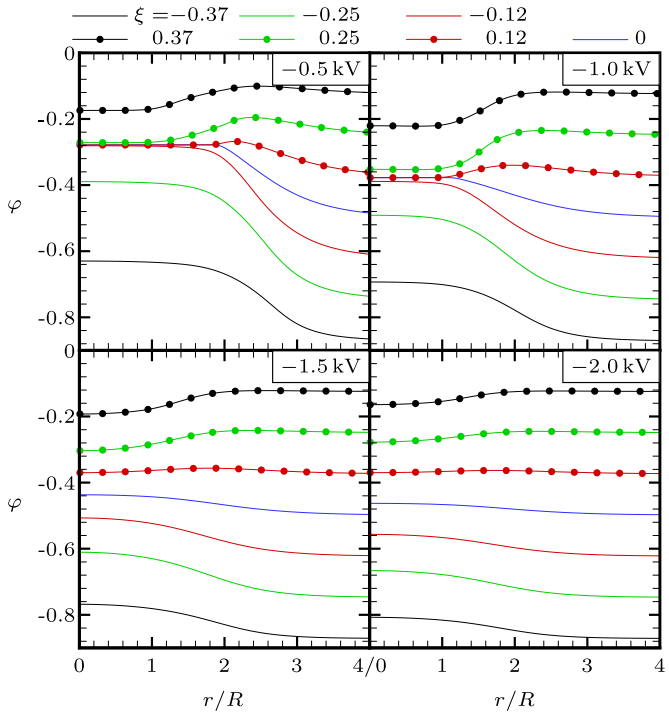

Fig. 7. Radial profiles of the normalized electric potential for the case $Z_{st} = 0.50$.

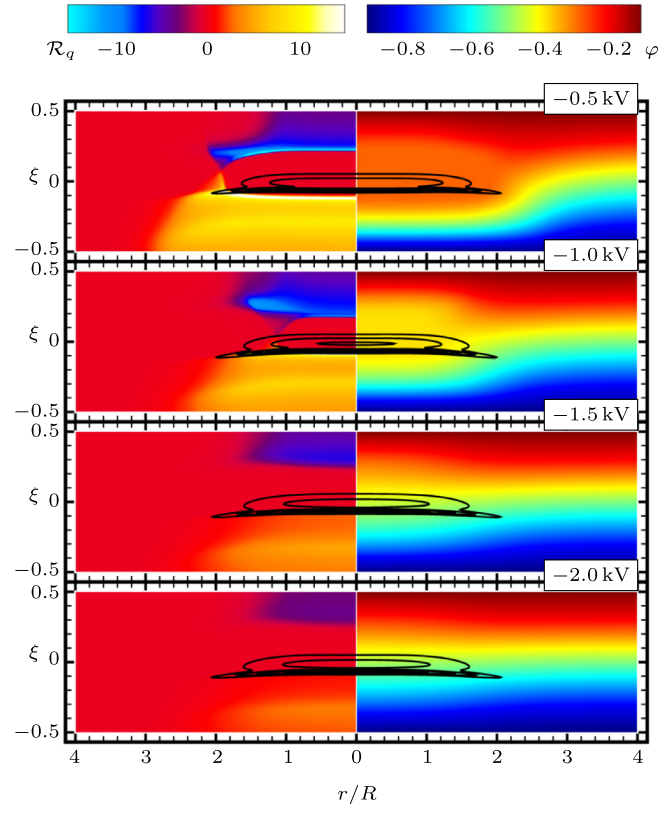

Fig. 8. Solid contours of the normalized total electric-charge density (left panels) and normalized electric potential (right panels) for the case $Z_{st} = 0.50$. Also included are isolines of the heat-release rate (dark lines).

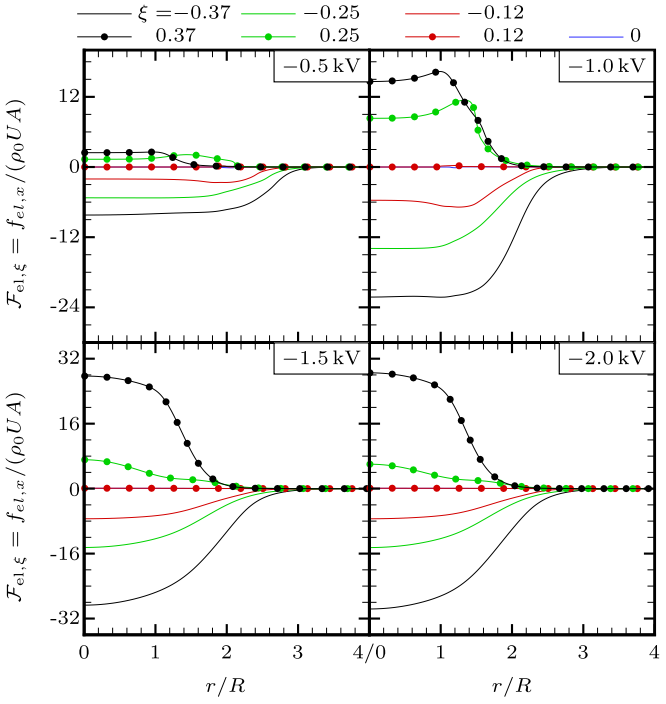

Fig. 9. Radial profiles of the normalized axial electric force for the case $Z_{st} = 0.50$.

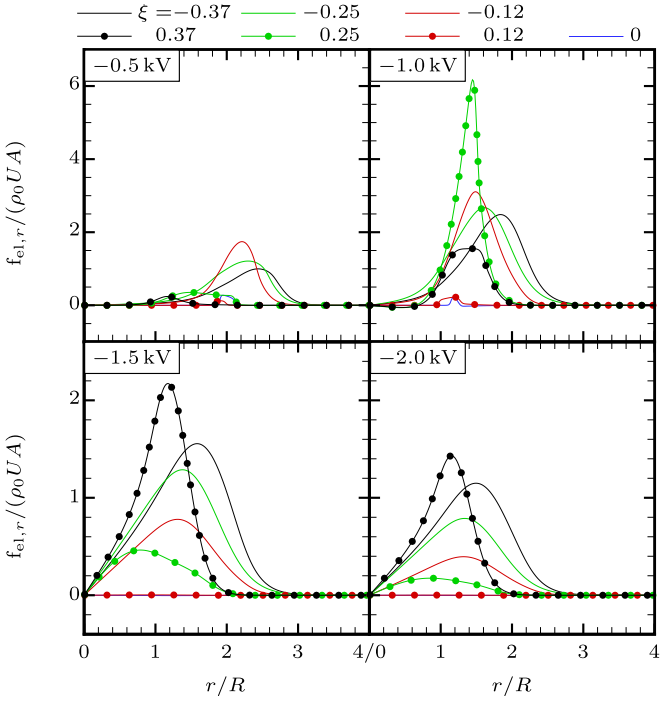

Fig. 10. Radial profiles of the normalized radial electric force for the case $Z_{st} = 0.50$.

The two aforementioned plateaus in the electric potential are bridged by an annular region where φ varies in the radial direction, which violates the necessary assumption for self-similarity that φ is a sole function of ξ. The two-dimensionality of the electric potential in the bridging region, which is clearly visible in the two upper right contour maps in Fig. 8, gives rise to a positive radial component of the electric force $f_{el,r}$, whose magnitude is also comparable to the characteristic convective force $\rho_0 UA$ albeit much smaller than the axial component $f_{el,x}$, as shown by comparing Figs. 9 and 10.

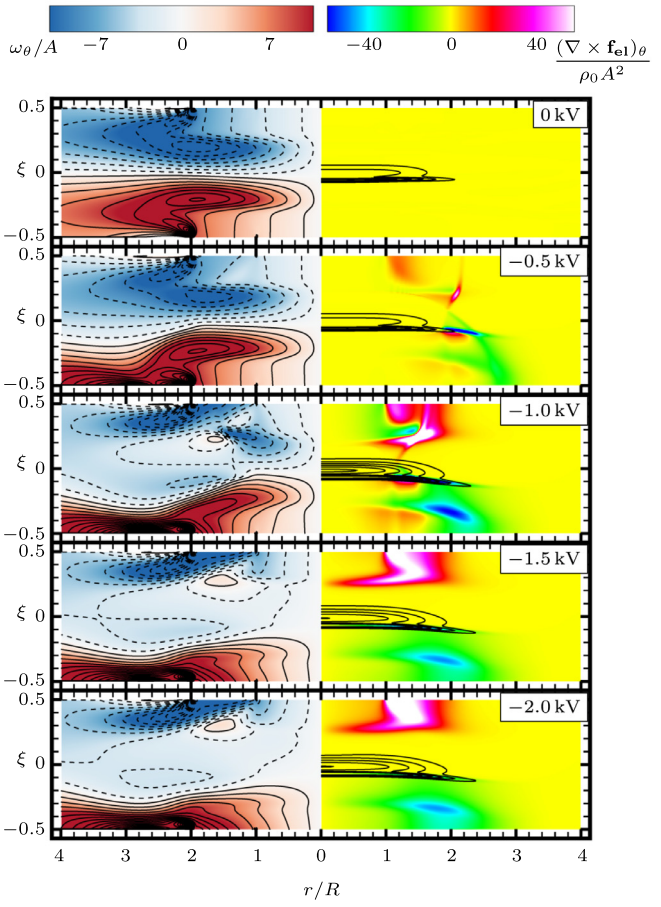

Fig. 11. Solid contours of the normalized azimuthal component of the vorticity (left panels) and of the normalized curl of the electric force (right panels) for the case $Z_{st} = 0.50$. Positive (negative) values of ω_θ correspond to anticlockwise (clockwise) vorticity. Solid and dashed isolines on the left panels indicate positive and negative isolines of vorticity, respectively. Solid lines on the right panels indicate isolines of the heat-release rate.

It is also in that bridging region where a strong two-dimensional gradient of charge density develops in the form of a curved lateral shield of electric charge, which, together with the flat portions of the shield above and below the diffusion flame, completely envelop the diffusion flame, as observed in the upper left panel in Fig. 8. Inside the resulting pancake-shaped Faraday cage, the magnitude of the electric field and the associated components of the electric force $f_{el,x}$ and $f_{el,r}$ are negligible. In contrast, the electric force is large along the edge of the charge shield, and more particularly, near its corners, where a strong misalignment exists between the gradients of the potential and the charge density.

The resulting electric-force map is a two-dimensional one in which the axial and radial forces are directed mostly outwards from the diffusion flame. The non-conservative character of the electric force emerging from the bridging region is clearly illustrated by the normalized contours of the azimuthal component of its curl $(\nabla\times\mathbf{f_{el}})_\theta/(\rho_0A^2)$ in the cases $\Delta\Phi_0 = -0.5$ kV and -1.0 kV shown in Fig. 11. Note that, if the gradient of the electric charge were aligned with the gradient of the potential everywhere, the electric force would be conservative and therefore irrotational everywhere, $(\nabla\times\mathbf{f_{el}})_\theta = 0$, which would make possible its absorption into the hydrodynamic pressure gradient as in Eq. (15). The sign of the vorticity source term $(\nabla\times\mathbf{f_{el}})_\theta$ observed in the results is such that it tends to abate the unelectrified distribution of vorticity that was originally present in the central region of the burner and was dominated by velocity gradients generated by thermal expansion and flow-entrance effects from the plug-flow boundary conditions (see left panels in Fig. 11). Similar characterizations of the effects of the electric force on the vorticity field under different injection-velocity boundary conditions represents an aspect worthy of future research.

In conclusion, at low voltages below saturation $|\Delta\Phi_0| \lesssim 1.0$ kV, the bridging region in the electric potential is located relatively far from the axis burner. Correspondingly, the electric force is mostly axial and radially uniform near the axis for $r/R \lesssim 1$, as observed in the two upper panels in Figs. 9 and 10. As a consequence, the electric force is mostly conservative there, as shown in the right panels corresponding to $\Delta\Phi_0 = -0.5$ kV and -1.0 kV in Fig. 11, and therefore does not lead to any significant momentum coupling. The flow is still adequately described by self-similarity, with the only caveat of the incipient non-uniformities in the axial distribution of the transformed pressure gradient, as shown in Figs. 3 and 6 for the cases $\Delta\Phi_0 = -0.5$ and -1.0 kV.

2.2.2. High voltages

To understand the breakdown of self-similarity in electrified conditions, it is illustrative to describe the transition undergone by the aerothermochemical field as the voltage increases from subsaturated to saturated conditions, which, in this burner, is also associated with the onset of a markedly two-dimensional character of the solution near the axis. In particular, as the saturation voltage is approached (e.g., see the $\Delta\Phi_0 = -1.0$ kV case in Figs. 6–9), the bridging region in the electric potential moves radially inwards. Consequently, the radial extension of the charge shield decreases as a result of an increased evacuation of charges by the electromigration flux, thereby leaving outer portions of the diffusion flame pierced by a nearly undisturbed electric field. The resulting radial profiles of $f_{el,r}$ are also shifted radially inwards, in such a way that the radial transfer of momentum becomes increasingly important in the vicinity of the axis.

At higher voltages into the saturated regime (e.g., see the $\Delta\Phi_0 = -1.5$ and -2.0 kV cases in Figs. 6–9), the prevailing electromigration flux has washed away the charge shield in all directions by steering the excess of charges toward the electrodes. The resulting electrostatic field is one in which the bridging region is broader and intercepts the burner axis, and across which the potential variation is small, thereby moderating the value of the radial electric force. The potential, which is slightly disturbed from its outer linear distribution by the diffusion flame because of the finite rate of charge electromigration, arrives with non-zero curvature at the burner axis. As a consequence, the radial component of the electric force rapidly transitions from zero value at the axis to a quantity of order $\rho_0 UA$ at $r/R \sim 1$, as shown in the lower right panel in Fig. 10. Similarly, the axial component of the electric force ceases to be uniform near the axis and varies parabolically in the radial direction, as observed in the lower right panel in Fig. 9. In this way, the electric force becomes non-conservative in the close vicinity of the axis (see panels corresponding to $\Delta\Phi_0 = -1.5$ kV and -2.0 kV in Fig. 11). It is the profuse two-dimensionality of the electric force near the burner axis in these high-voltage conditions that induces a significant non-linear scaling of the radial pressure gradient, axial variations of J, along with radial variations on the velocity components $\mathcal{U}$ and $\mathcal{A}$, and consequently, on ΘA, and Y_i, thereby breaking down the self-similarity. At these high voltages, the electric force cannot be passively absorbed into the hydrodynamic pressure gradient and has a dynamical effect on the velocity field that leads to significant momentum coupling.

It is worth mentioning that the radial electric force $f_{el,r}$ follows a linear scaling with r near $r = 0$, as shown in the transformed

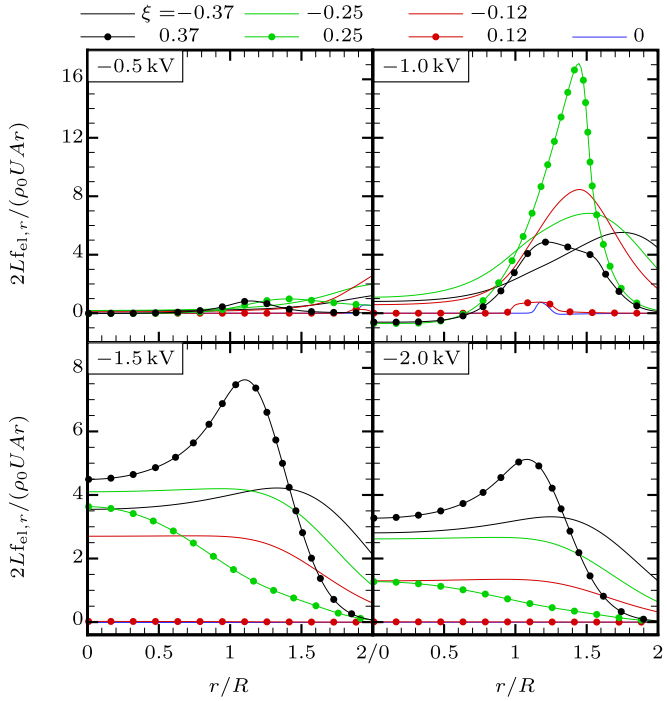

Fig. 12. Radial profiles of the transformed radial electric force for the case $Z_{st} = 0.50$.

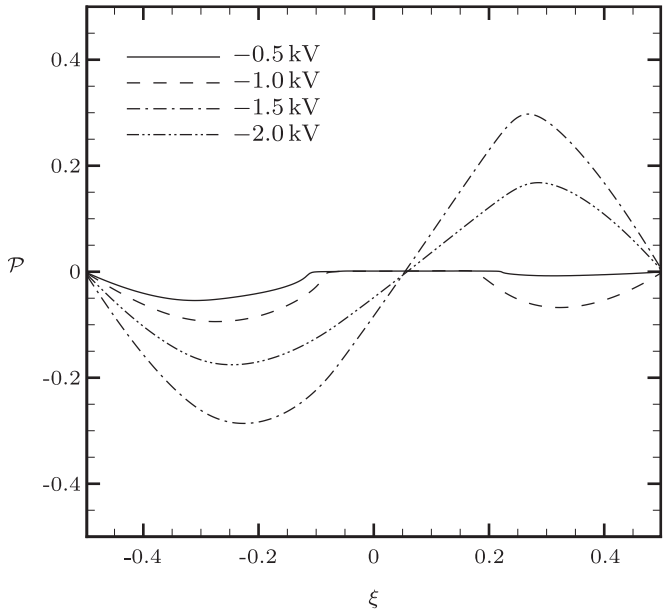

Fig. 13. Axial distribution of the dimensionless radial curvature of the electric potential at the axis $r = 0$ for the case $Z_{st} = 0.50$.

profiles in Fig. 12. Therefore, in order to palliate some of the shortcomings of the formulation (1)–(13), it would be tempting to include a transformed radial electric force $\mathcal{F}_{el,r}(\xi) = 2f_{el,r}L/(\rho_0 UAr)$ on the right-hand side of the transformed radial momentum equation (2) while limiting the self-similar description to very small radial distances $r \to 0$, with $f_{el,r}/r$ being finite in that limit. In principle, at high voltages, this addition would create a positive source of momentum in the radial direction in Eq. (2) that would consequently increase the axial velocity toward the stagnation plane by mass conservation. Note that these dynamics would be opposite to those observed in the experiments [6] and simulations [1], in which the axial flow toward the stagnation plane is decelerated in electrified conditions. The discrepancy would be partially palliated by employing the precomputed parabolic-like distribution of the pressure gradient $J(\xi)$ (see Fig. 6) in solving Eq. (2), but that would be of limited practical interest. In addition, the transformed radial electric force

$$\mathcal{F}_{el,r}(\xi) = \frac{2Lf_{el,r}}{\rho_0 UAr} = -\Xi_M \sum_{i=1}^{N_s} \mathcal{P}\mathcal{R}_{q,i}(\xi) \tag{17}$$

would necessarily involve the non-zero radial curvature $\mathcal{P}$ of the electric potential defined by its quadratic expansion near the axis,

$$\varphi = \phi(\xi) + \frac{\mathcal{P}}{4}\left(\frac{r}{L}\right)^2. \tag{18}$$

As observed in Fig. 13, the curvature of the potential is an oscillatory function of ξ that becomes zero near the flame axial location and at the boundaries $\xi = \pm 1/2$, where the quadratic expansion (18) must satisfy the Dirichlet boundary conditions for φ at the electrodes (i.e., $\varphi = 0$ at $\xi = 1/2$, and $\varphi = -1$ at $\xi = -1/2$). It can be shown that the utilization of (18) in deriving a revised self-similar formulation would lead to additional terms involving $\mathcal{P}(\xi)$ that would appear in the transformed versions of the species and energy conservation equations, as well as in the Gauss equation. However, similarly to $J(\xi)$, the function $\mathcal{P}(\xi)$ would need to be precomputed numerically from a full numerical simulation of the type reported in Ref. [1]. Note that, even if the exact $J(\xi)$ and $\mathcal{P}(\xi)$ were to be substituted into the self-similar formulation augmented with the terms mentioned above, the solution to the resulting system of equations along the axis might differ from the solution provided by the full numerical simulations. This can be understood by noticing that the velocity components $\mathcal{A}$ and $\mathcal{U}$ also develop an increased two-dimensional character with increasing voltages, and that near the axis they are better described by series expansions in even powers of r. The second-order coefficients of those expansions, or equivalently, the radial curvatures of $\mathcal{A}$ and $\mathcal{U}$, would readily appear in the viscous terms of the transformed momentum equations in the radial and axial directions, thereby complicating the analysis in a multi-fold manner and leading to the inconvenience of having to precompute additional unclosed functions using full numerical simulations.

3. Conclusions

Based on the above considerations, it is concluded that self-similar descriptions are appropriate in this counterflow configuration under zero incident electric fields. However, in electrified conditions, the self-similar description breaks down because of two-dimensional electrohydrodynamic effects associated with transition from sub-saturated to saturated conditions. These effects lead to a transition between a mostly axial and conservative electric force field, which has a small magnitude and is directed away from the diffusion flame, to a biaxial and non-conservative electric force field of larger magnitude at higher voltages. In the latter conditions, a radial component of the electric force pervasively influences the vicinity of the axis in conjunction with a large outwards axial electric force that corresponds to a bi-directional ionic wind. The resulting two-dimensional and non-conservative character of the electric force prevents from passively absorbing it into the gradient of the hydrodynamic pressure. It also induces significant non-linear scaling of the radial pressure gradient, large axial variations of the radial pressure gradient, along with radial variations on the axial velocity, temperature and mass fractions, thereby breaking down the self-similarity.

The breakdown described above occurs more profusely under undiluted injection conditions corresponding to pure methane

burning in air (i.e., $Z_{st} = 0.07$). In this case, the diffusion flame is located closer to the oxidizer injector and acquires a significant concave curvature in unelectrified conditions (e.g., see Fig. 10(b) in Ref. [1]), which induces large radial variations in all variables. As shown in the figures provided in the Supplementary Material accompanying this paper, the numerical results indicate that the configuration with $Z_{st} = 0.07$ cannot be described by self-similar formulations in any of the cases analyzed here, including the one where there is no incident electric field.

In unelectrified conditions, it is known that self-similarity in counterflow diffusion flames can be preserved by using sufficiently slender burners with large aspect ratios $2R/L \gg 1$. The present study suggests that, all other characteristics of the configuration being the same, the aspect ratio required to preserve self-similarity in electrified conditions is larger than the aspect ratio required to satisfy that condition in the absence of electric fields. This difference is caused by two-dimensional electrohydrodynamic flow distortions generated at the edges of the diffusion flame, which creep radially toward the axis in a noticeable manner due to the elliptic character of the electrostatic field. In principle, extra-large aspect ratios are expected to maintain radial uniformity in the electric and aerothermochemical fields for as much radial distance as possible, thereby leading to an axial and conservative electric force that could be passively absorbed into the hydrodynamic pressure gradient without any dynamical consequences. As a result, in that slender limit, the ionic wind would be mostly axial and radially uniform, the strong momentum coupling observed in experiments [6] and simulations [1,7] would disappear, the intensity across the burner would vary monotonically with the voltage, and the self-similar description (1)–(13), including its counterpart in flamelet model form [25], would perhaps be useful in describing the flow field. Further research would be worthwhile for an improved understanding of these aspects, possibly in configurations animated by higher Reynolds numbers for enhanced separation of scales.

Acknowledgments

This investigation was supported by the US AFOSR Grant # FA9550-14-1-0219, the Italian MIUR Grant # PON03PE_00067_6 APULIA SPACE, and the US DoE/NNSA Grant # DE-NA0002373 as part of the Stanford PSAAP-II Center. Javier Urzay is grateful to Prof. Fabrizio Bisetti for motivating the question addressed in this study during his visit to Stanford in 2011. This work was performed during the visit of Mario Di Renzo to the Stanford University Center for Turbulence Research in Fall 2016 and Winter 2017.

Supplementary material

Supplementary material associated with this article can be found, in the online version, at doi:10.1016/j.combustflame.2019.04.004.

References

[1] M.D. Renzo, J. Urzay, P. De Palma, M.D. de Tullio, G. Pascazio, The effects of incident electric fields on counterflow diffusion flames, Combust. Flame 193 (2018) 177–191.
[2] E. Sher, G. Pinhasi, A. Pokryvailo, R. Bar-On, Extinction of pool flames by means of a DC electric field, Combust. Flame 94 (1993) 244–252.
[3] A.R. Hutchins, W.A. Reach, J.D. Kribs, K.M. Lyons, Effects of electric fields on stabilized lifted propane flames, J. Energy Resour. Technol. 136 (2014) 1–10.
[4] A. Cessou, E. Varea, K. Criner, G. Godard, P. Vervisch, Simultaneous measurements of OH, mixture fraction and velocity fields to investigate flame stabilization enhancement by electric field, Exp. Fluids 52 (2012) 905–917.
[5] F. Borgatelli, D. Dunn-Rankin, Behavior of a small diffusion flame as an electrically active component in a high-voltage circuit, Combust. Flame 159 (2012) 210–220.
[6] D.G. Park, S.H. Chung, M.S. Cha, Bidirectional ionic wind in nonpremixed counterflow flames with DC electric fields, Combust. Flame 168 (2016) 138–146.
[7] M. Belhi, B.J. Lee, F. Bisetti, H.G. Im, A computational study of the effects of DC electric fields on non-premixed counterflow methane–air flames, J. Phys. D: Appl. Phys. 50 (2017) 494005.
[8] A. Liñán, The asymptotic structure of counterflow diffusion flames for large activation energies, Acta Astronaut. 1 (1974) 1007–1039.
[9] N. Peters, Turbulent Combustion, Cambridge University Press, 2004.
[10] H. Pitsch, N. Peters, A consistent flamelet formulation for non-premixed combustion considering differential diffusion effects, Combust. Flame 114 (1998) 26–40.
[11] C.D. Pierce, P. Moin, Progress-variable approach for large-eddy simulation of non-premixed turbulent combustion, J. Fluid Mech. 504 (2004) 73–97.
[12] J. Urzay, Supersonic combustion in air-breathing propulsion systems for hypersonic flight, Annu. Rev. Fluid Mech. 50 (2018) 593–627.
[13] A. Liñán, D. Martínez-Ruiz, A.L. Sánchez, J. Urzay, Regimes of spray vaporization and combustion in counterflow configurations, Combust. Sci. Technol. 187 (2015) 103–131.
[14] A.D. Weiss, W. Coenen, A.L. Sánchez, Aerodynamics of planar counterflowing jets, J. Fluid Mech. 821 (2017) 1–30.
[15] J. Carpio, A. Liñán, A.L. Sánchez, F.A. Williams, Aerodynamics of axisymmetric counterflowing jets, Combust. Flame 177 (2017) 137–143.
[16] K. Seshadri, F.A. Williams, Laminar flow between parallel plates with injection of a reactant at high Reynolds number, Int. J. Heat Mass Transf. 21 (1978) 251–253.
[17] L. Krishnamurthy, F.A. Williams, K. Seshadri, Asymptotic theory of diffusion-flame extinction in the stagnation-point boundary layer, Combust. Flame 26 (1976) 363–377.
[18] S.C. Li, Spray stagnation flames, Progr. Energy Combust. Sci. 23 (1997) 303–347.
[19] U. Niemann, K. Seshadri, F.A. Williams, Accuracies of laminar counterflow flame experiments, Combust. Flame 162 (2015) 1540–1549.
[20] M.D. Smooke, P. Lin, J.K. Lam, M.B. Long, Computational and experimental study of a laminar axisymmetric methane–air diffusion flame, Symp. (Int.) Combust. 23 (1991) 575–582.
[21] M.D. Smooke (Ed.), Reduced Kinetic Mechanisms and Asymptotic Approximations for Methane–Air Flames, 384, Lecture Notes in Physics, Springer-Verlag, Berlin/Heidelberg (1991).
[22] C.E. Frouzakis, J. Lee, A.G. Tomboulides, K. Boulouchos, Two-dimensional direct numerical simulation of opposed-jet hydrogen-air diffusion flame, Symp. (Int.) Combust. 27 (1998) 571–577.
[23] V. Mittal, H. Pitsch, F. Egolfopoulos, Assessment of counterflow to measure laminar burning velocities using direct numerical simulations, Combust. Theory Model. 16 (2012) 419–433.
[24] R.F. Johnson, A.C. Vandine, G.L. Esposito, H.K. Chelliah, On the axisymmetric counterflow flame simulations: is there an optimal nozzle diameter and separation distance to apply quasi one-dimensional theory? Combust. Sci. Technol. 187 (2015) 37–59.
[25] M.D. Renzo, P. De Palma, M.D. de Tullio, G. Pascazio, An efficient flamelet progress-variable method for modeling non-premixed flames in weak electric fields, Comput. Fluids 157 (2017) 14–27.